Available online at www.sciencedirect.com
SCIENCE DIRECT®
International Journal of Heat and Fluid Flow 25 (2004) 180–195
International Journal of
HEAT AND FLUID FLOW
www.elsevier.com/locate/ijhff

Interferometric and numerical study of the temperature field in the boundary layer and heat transfer in subcooled flow boiling

Anita Lucic [a,*], Maximilian Emans [b], Franz Mayinger [a], Christoph Zenger [b]

[a] *Lehrstuhl für Thermodynamik, Technische Universität München, Boltzmannstrasse 15, 85747 Garching, Germany*
[b] *Lehrstuhl für Informatik V, Technische Universität München, Boltzmannstrasse 15, 85747 Garching, Germany*

Abstract

An interferometric study and a numerical simulation are presented of the combined process of the bulk turbulent convection and the dynamic of a vapor bubble which is formed in the superheated boundary layer of a subcooled flowing liquid, in order to determine the heat transfer to the flowing subcooled liquid. In this investigation focus has been given on a single vapor bubble at a defined cavity site to provide reproducible conditions. In the experimental study single bubbles were generated at a single artificial cavity by means of a CO_2-laser as a spot heater at a uniformly heated wall of a vertical rectangular channel with water as the test fluid. The experiments were performed at various degrees of subcooling and mass flow rates. The bubble growth and the temporal decrease of the bubble volume were captured by means of the high-speed cinematography. The thermal boundary layer and the temperature field at the phase-interface between fluid and bubble were visualized by means of the optical measurement method holographic interferometry with a high temporal and spatial resolution, and thus the local and temporal heat transfer could be quantified. The experimental results form a significant data basis for the description of the mean as well as the local heat transfer as a function of the flow conditions. According to the experimental configuration and the obtained data the numerical simulations were performed. A numerical method has been developed to simulate the influence of single bubbles on the surrounding fluid which is based on a Lagrangian approach to describe the motion of the bubbles. The method is coupled to a large-eddy simulations by the body force term which is locally evaluated based on the density field. The obtained experimental data correspond well with the numerical predictions, both of which demonstrate the thermo- and fluiddynamic characteristics of the interaction between the vapor bubble and the subcooled liquid.

Keywords: Holographic interferometry; Thermal boundary layer; Bubble dynamics; Local heat transfer; Euler-Lagrange model; Force-coupling method

1. Introduction

Subcooled flow boiling, which is a complex process combining thermo- and fluiddynamic characteristics, plays an important role in a multitude of technical applications owing to the significant enhancement of heat transfer compared to single-phase forced convection. This is due to two major effects, namely the detachment process of the bubble from the heated surface at which superheated fluid layers are dragged into and mixed with the subcooled fluid and thus generating microscopic turbulence, as well as the decrease of the bubble volume and bubble collapse releasing the stored energy within the bubble.

The determination of the various heat transfer mechanisms and their contribution to the overall heat transfer has been subject of extensive research efforts, but due to its complexity there is still a lack of available experimental data and reliable models. The process of subcooled flow boiling is governed by the interaction of multiple physical parameters such as the temperature gradient in the thermal boundary layer, the flow pattern and turbulence of the liquid phase as well as by the thermal and fluiddynamic behavior of the vapor bubble. The bubble dynamics and the superheated thermal boundary layer continuously affect each other. The condition of the boundary layer is determined by the nucleation and the bubble growth, and on the other

---

[*] Corresponding author.
E-mail address: lucic@td.mcu.tum.de (A. Lucic).

0142-727X/$ - see front matter © 2003 Elsevier Inc. All rights reserved.
doi:10.1016/j.ijheatfluidflow.2003.11.004

hand the temperature gradient in the boundary layer has an impact on the bubble growth and condensation.

For a detailed understanding of the interaction between the thermal liquid boundary layer and a vapor bubble with respect to the heat transfer the knowledge of global parameters is not sufficient. It is of major importance to analyze the growth of a single vapor bubble in the temperature field of the superheated boundary layer as well as the momentary condition of the thermal boundary layer, and the dynamic process of the detachment and volume decrease with the resulting microscopic turbulence in the liquid.

For this investigation the non-invasive measurement technique of the holographic interferometry represents a reliable tool. It is advantageous in measuring and visualizing very thin boundary layers and temperature fields in transient and fast processes such as in turbulent flows, where the application of conventional methods is very limited.

So far interferometric studies on the temperature field and the heat transfer at the phase-interface of single bubbles in subcooled liquids have mainly been performed within a very limited parameter range by eliminating the impact of the forced convection and/or the impact of the thermal boundary layer in order to provide manageable experimental conditions, as it is shown by Chen (1985), Nordmann and Mayinger (1981), Qiu and Dhir (1999) and Van Helden (1994). Therefore there is a need for further experimental investigations which are specifically directed towards determining the combined process of a vapor bubble growing in the superheated thermal liquid layer and the forced bulk convection. As it will be shown subsequently, the holographic interferometry has been successfully applied to visualize the temperature field and hence to determine the heat transfer coefficient at the phase-interface.

Parallel to the experimental work a numerical method has been developed which can be applied to calculate the flow field and the temperature distribution in configurations such as the ones studied in the experiments. For numerical simulations two main problems have to be solved: first turbulence either has to be simulated directly or modeled, second an appropriate way for the description of the time-variant shape of the phase-interface has to be found. Simulation of turbulence and the description of the phase-interface have to match as well as possible in terms of both, accuracy and computational costs.

Today turbulence can be simulated directly, i.e. without the application of any other mathematical model but the Navier–Stokes equations. Results of simulations of single-phase problems obtained by such methods are considered to be as accurate as experiments. However, finding an appropriate extension for the simulation of two-phase problems is anything but straight forward. Nevertheless, there are methods which allow DNS for two-phase flows, these rely on modeling of the phenomena on the phase-interface. Tryggvason et al. (2001) describe a front-tracking method which is based on the description of the surface shape by a grid spanned by particles transported by the flow field. There are several successful simulations employing this method reported now in literature, e.g. Esmaeeli and Tryggvason (1998, 1999) and Göz et al. (2002). However, the computational costs of this method are very high, therefore the method is still restricted to the simulation of only a few bubbles, and the use of high-performance computers is indispensable. There are also DNS reported where the influence of the gas phase is modeled by Volume-of-Fluid methods (first mentioned in literature by Hirt and Nichols (1981)), e.g. Kanai and Miyata (2001).

In cases in which no supercomputers are to be employed, the simulation of turbulent flows requires a certain amount of modeling. $k - \varepsilon$ models can greatly reduce the calculation cost, however, these savings coincide with a loss of accuracy. In the field of two-phase flows these turbulence models are reported to yield reliable results when combined with volume-averaging methods, e.g. Socholichin and Eigenberger (1994, 1999). But averaging means that the shape and position of the phase-interface is no longer calculated.

For the purpose of simulation of the effects in the vicinity of a heated wall it is important to know the shape and the position of the phase-interface as exactly as possible. If, on the other hand, the computational costs are to be kept within a reasonable frame, DNS is not suitable. On modern personal computers large-eddy simulations (LES) with a reasonable spatial resolution can be performed. Both, front-tracking methods and volume-of-fluid methods could possibly be linked to LES as well, but we shall demonstrate that for our purpose it is possible to apply a method based on a Lagrangian description of the bubbles which proves to be very efficient. By modeling the major effects of the bubble on the fluid field we yield accurate predictions of both, flow field and bubble motion.

2. Experimental techniques

2.1. Experimental set-up

A schematic diagram of the experimental facility used for the investigation of the temperature field and heat transfer in subcooled flow boiling is shown in Fig. 1.

Water is used as the test fluid and is circulated through the loop by means of a magnetically coupled centrifugal pump, which delivers a constant volumetric flow. The fluid is then directed through a preheater. The preheated volumetric flow is divided into a main stream

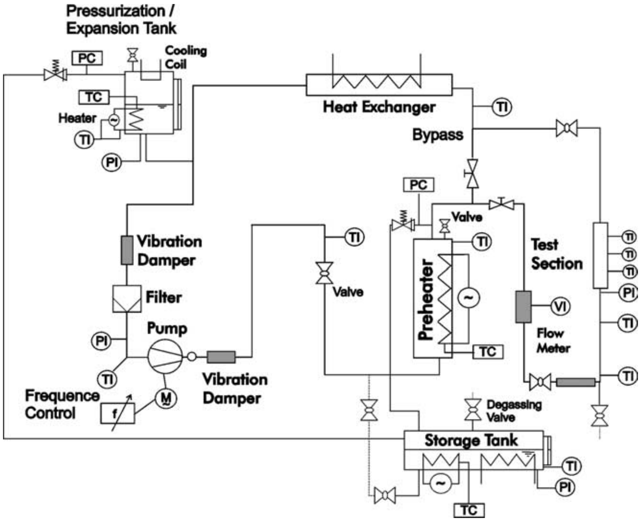

Fig. 1. Experimental set-up.

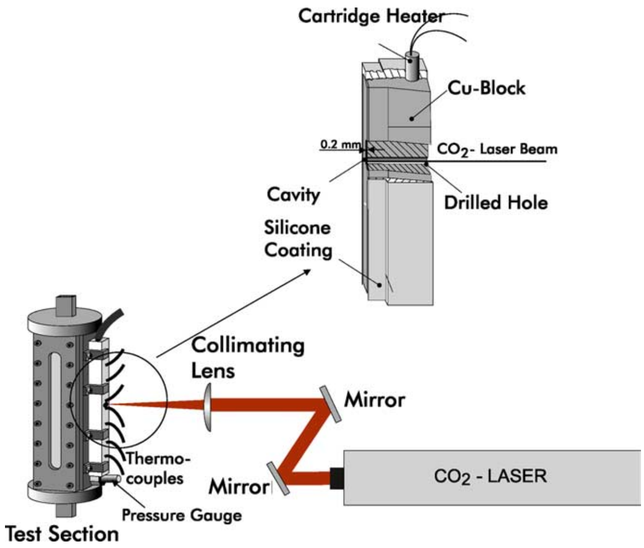

Fig. 2. Test section and optical set-up for spot heating with the CO_2-laser.

and into a bypass stream which are regulated by manually operated valves. The main stream passes the test section. Having passed the test section the main stream merges into the bypass stream and is cooled down by a condenser before returning to the pump. By means of the pressurization tank which is attached at the highest position of the loop a constant system pressure up to 5 bar can be realized. It also functions as an expansion vessel for the heated fluid. Furthermore a storage tank is connected to the loop in which the water is degassed before entering the loop.

Before conducting the experiments an operating pressure of 1.1 bar absolute in the test section is achieved by heating the pressurization tank. By setting the valves of the main and bypass stream, the volumetric flow through the test section is regulated and maintained. The volumetric flow of the main stream is measured and displayed by means of a magnetically inductive flow meter. The volumetric flow is heated up to a certain inlet temperature which, according to the measurement condition, is few degrees below the saturation temperature of the corresponding operating pressure. The setting and the regulation of the fluid temperature is achieved by a heat output control which provides a constant fluid temperature in a steady state condition at a constant heat output. In order to avoid heat losses, all the following pipes behind the preheater as well as the test section are insulated.

The test section is composed of a vertically aligned rectangular channel that has a cross-section of 8 mm × 10 mm. The test section is depicted in Fig. 2. The length of the test section is 334 mm. In order to ensure a fully developed flow, an inlet section of 550 mm which corresponds to a ratio of $L/D_{\mathrm{hyd}} = 61$ and an outlet section of 350 mm which corresponds to a ratio of $L/D_{\mathrm{hyd}} = 39$ are realized.

The body of the test section consists of stainless steel. The four test section walls are inserted into the body and are sealed by using O-ring seals and silicone. Three of the walls comprise a glass insert to provide optical measurements. The heatable copper block is adjusted in one-side of the test section body whose front wall is polished. The polished surface serves the purpose of eliminating cavities that are engendered by the roughness.

The artificial cavity was generated by exerting a YAK-laser to the polished copper surface. The copper block is heated by means of cartridge heaters, and it is insulated with silicone coating and glass wool to prevent heat loss. The artificial cavity is additionally spot heated by means of a CO_2-laser in order to induce nucleation only at this cavity, whereas the thermal boundary layer is realized by uniformly heating the surface with the cartridge heaters. At the back of the copper block a drilled hole was made in axial direction towards the artificial cavity that ends at a distance of 0.2 mm before the cavity. This drilled hole serves as the passage for the laser beam which has, at the inlet of the drilled hole, a diameter of 0.2 mm. The laser beam is focussed on the spot of the cavity by means of mirrors and a collimating lens, as it is also illustrated in Fig. 2.

For the acquisition of the signals of both the thermocouples and pressure gauges which are located at various spots in the loop as well as in the test section, a multiprogrammer by Hewlett Packard was used which exchanges data via HP-IB communication with the PC. Within the copper block seven thermocouples are inserted at various heights at a distance of 0.1 mm from the polished surface which enables temperature measurements along the heater surface. The temperature at the copper surface is set and controlled by means of a temperature control. A self-programmed HP-Vee programm calculates the degree of subcooling of the flowing water as well as the superheat of the heated wall compared to the saturation temperature.

2.2. Holographic interferometry

The holographic interferometry has been applied in various fields of heat transfer phenomena both in single-phase and two-phase flow. A significant advantage of the holographic interferometry, like other optical measurement methods, is the non-invasive mode of investigating the physical process of interest. This inertialess method in combination with the high-speed cinematography enables the study of the temperature fields in transient and extremely fast processes.

The theory of the holographic interferometry is very comprehensive, and therefore only the basic principle will be explained in this paper. Detailed information about the holographic interferometry in general can be found in Chen (1985), Grigull and Hauf (1970), Hauf et al. (1991), Mayinger (2000), Nordmann and Mayinger (1981) and Panknin (1977).

The holographic interferometry technique is based upon the principle of the recording and storing method of holography, as introduced and described by Gabor (1951).

The laser beam is divided by means of a beam splitter into an object wave and into a reference wave each of which is then expanded and collimated by means of a beam expansion system comprising a microscopic lens and a collimating lens, as it can be seen from the optical set-up of the holographic interferometry in Fig. 3. The object wave is stored on a holographic plate after having passed the test section where the transport process has not been activated yet, while the expanded reference wave circumvents the test section. Both waves are superimposed on the holographic plate. By illuminating the holographic plate, which is developed after the recording, with the reference beam the object beam can be reconstructed.

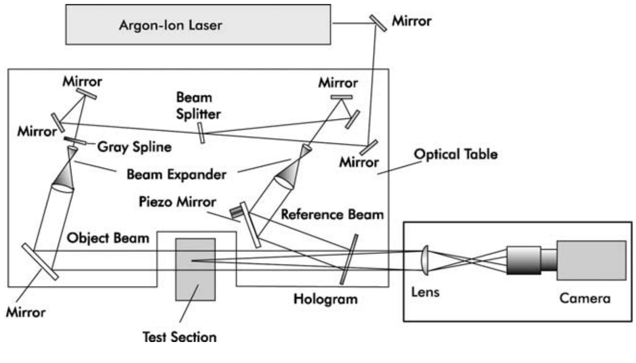

Fig. 3. Optical set-up for the holographic interferometry.

The onset of such a transport process results in a density gradient and thus in a refractive index gradient due to the formed temperature field. Owing to this change of the refractive index field, the object wave that passes through the test section is subjected to a phase shift. By reconstructing the recorded hologram with the reference beam in the original condition, the momentary object wave and the original object wave, which is the comparison wave, interfere with each other due to the phase shift. By means of the interference fringes the temperature distribution and thus the heat transfer coefficient can be determined.

For the investigation of the heat transfer the *real-time method* was used which enables a continuous recording and observing of the transport processes in the fluid. In this method only the original object wave (comparison wave) passing the measurement region before the onset of the heat transfer process is stored on a hologram. After the development the hologram is repositioned accurately in its initial position in the plate holder. By illuminating the hologram with the reference wave, a continuous reconstruction of the comparison wave and thus of the original condition in the test section is realized. If the condition in the test section does not differ from the condition at the point of time of the hologram exposure, the hologram will not show any interference fringes which is called the *infinite-fringe method.*

As already mentioned, at the onset of the heat transfer process, the object wave is subjected to a phase shift due to the temperature gradient in the test section, and it is superimposed by the reconstructed comparison wave on the hologram. This superimposition of the momentary object wave and the reconstructed original object wave results in an interference pattern which can be observed and filmed continuously.

The determination of density gradients can also be realized by the *finite-fringe method* which is applied when investigating thin boundary layers. In this region the interference fringe density is very high, and the evaluation with the infinite-fringe method becomes very difficult. In this method parallel interference fringes are generated on the reference hologram before the transport process is activated. This pattern is realized by displacing the reference beam within a few wave lengths by means of the piezo-mirror. The direction and the fringe density is set by the movement of the mirror. With the onset of the transport process these parallel fringes are deflected which is a measure for the density gradient and therefore for the temperature gradient.

2.2.1. Evaluation of the interferograms

As already described, the principle of the holographic interferometry is based on the physical effect of interference which is the superposition of two light waves one of which is phase shifted. The phase shift results from the different optical path lengths traversed by the object and comparison wave. The phase shift of the light wave can be expressed by a multiple S of the wave length λ, while the optical path length is defined by the product of the refractive index and the geometric path length. Therefore, the equation of the ideal interferometry is defined by

$$S(x,y)\cdot\lambda = l\cdot[n_\infty - n(x,y)] \tag{2.1}$$

With the refractive index as a function of the temperature $\mathrm{d}n/\mathrm{d}T$ the correlation between interference field and temperature field can be determined from Eq. (2.1).

$$S(x,y)\cdot\lambda = l\cdot\frac{\mathrm{d}n}{\mathrm{d}T}\cdot[T(x,y) - T_\infty] \tag{2.2}$$

By using Eq. (2.2) the respective interference fringes, whose distance from the heated wall are measured from the interferogram, can be converted into temperatures which are then plotted versus the distance from the heated wall, as it is depicted in Fig. 4.

The temperature profile $T(y)$ of the flowing liquid is obtained and the heat transfer between the heated wall and the flowing liquid can be determined. Hereby, the temperature gradient $(\mathrm{d}T/\mathrm{d}y)_\mathrm{W}$ in the immediate vicinity of the wall is the governing parameter, since in this point the energy is transferred according to Fourier's law of heat conduction due to the non-slip condition between the heated wall and the fluid. By equating the Fourier's law of heat conduction and the Newton's equation of convective heat transfer the local heat transfer coefficient can be calculated:

$$\alpha(x) = -\frac{\lambda_\mathrm{F}\cdot\left(\frac{\mathrm{d}T}{\mathrm{d}y}\right)_\mathrm{W}}{T_\mathrm{W} - T_\mathrm{F}} \tag{2.3}$$

The temperature gradient at the wall is determined by approximating the interferometrically measured temperature distribution with a polynome function which is then differentiated with setting $y = 0$.

The local Nusselt number is then calculated as follows:

$$Nu(x) = \frac{\alpha(x)\cdot x}{\lambda_\mathrm{F}} \tag{2.4}$$

The temperature difference $T_\mathrm{W} - T_\mathrm{F}$ in Eq. (2.3) is defined as the temperature difference between the heated wall and the subcooled fluid in the test section.

For the evaluation of the interferograms in the immediate vicinity of vapor bubbles, Eq. (2.1) cannot be solved as described, since the assumptions of the ideal interferometry—constant value of n along the optical path and no deflection of the light beam along the temperature field—do not apply. In the case of rotationally symmetrical temperature fields the refractive index changes along the axial direction of the beam according to an unknown function. For this reason the determination of bended temperature fields requires the inversion of the integral. As a result the Abel-Integral, as described in Grigull and Hauf (1970), and Hauf et al. (1991) is obtained which considers the varying optical paths of the light beam when penetrating rotationally symmetrical bodies.

$$\Delta n(r) = -\frac{\lambda_0}{\pi}\int_r^{r_0}\frac{\mathrm{d}S(y/\mathrm{d}y)}{\sqrt{y^2 - r^2}}\,\mathrm{d}y \tag{2.5}$$

The correlation incorporates the measured fringe order S and its differentiation, respectively, which is a function of y, and the refractive index which in turn is a function of the radial distance of the bubble- or the spherical surface, respectively.

However, when evaluating the temperature field around vapor bubbles, it has to be considered that the light beams are subjected to major deflections when passing the temperature field of the bubble due to the very high local temperature gradients in the thermal boundary layer which is demonstrated in Fig. 5.

For the determination of this deflection a complicated correction procedure has been used which is described by Chen and Mayinger (1985, 1992) and by Nordmann and Mayinger (1981). In this calculation procedure the deflection is corrected, and the temperature profile

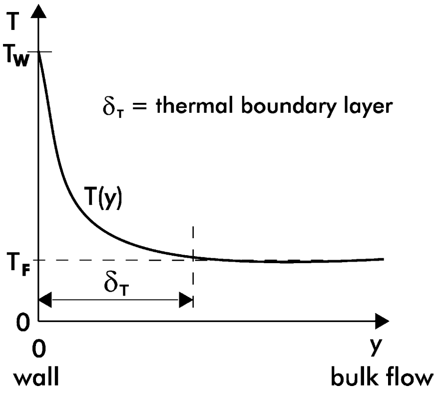

Fig. 4. Temperature distribution $T(y)$ of a flowing liquid versus the distance y of the heated wall.

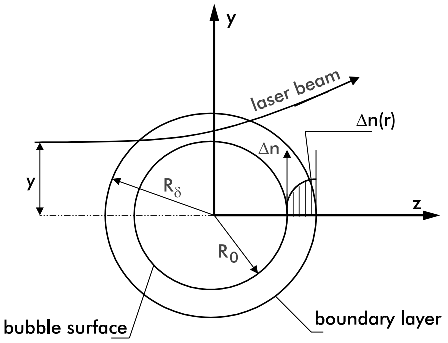

Fig. 5. Deflection of the light beam in the temperature field around a spherical bubble.

around the bubble is approximated by a polynome function.

3. Experimental results

3.1. Visualization of the thermal boundary layer in single-phase forced convection

Before discussing the interaction between bubble dynamics and thermal boundary layer of the flowing liquid, the formation of the thermal boundary layer at the heated test section wall at single-phase convection is presented. The temperature gradient in the thermal boundary layer, namely, governs the bubble formation and growth. Fig. 6 shows two interferograms according to the infinite-fringe method, as described before, of the flow at various fluid velocities yet at approximately equal inlet temperatures. The mean liquid velocities are 0.22 and 0.3 m/s which correspond to a Reynolds number of 6500 and 8700, respectively, based on the hydraulic diameter and the mean liquid velocity.

Each interference fringe corresponds to an isotherm. Therefore, the temperature distribution in the thermal boundary layer can be determined from the measured wall and the fluid temperature. The distance between two fringes corresponds to the temperature difference dT/dS which is calculated from Eq. (2.2). The temperature gradient dT/dy increases with increasing the fringe density. It is discernible that the fringe density increases towards the wall. It can also be seen that the thermal boundary layer of the higher Reynolds number is thinner than that of the lower Reynolds number.

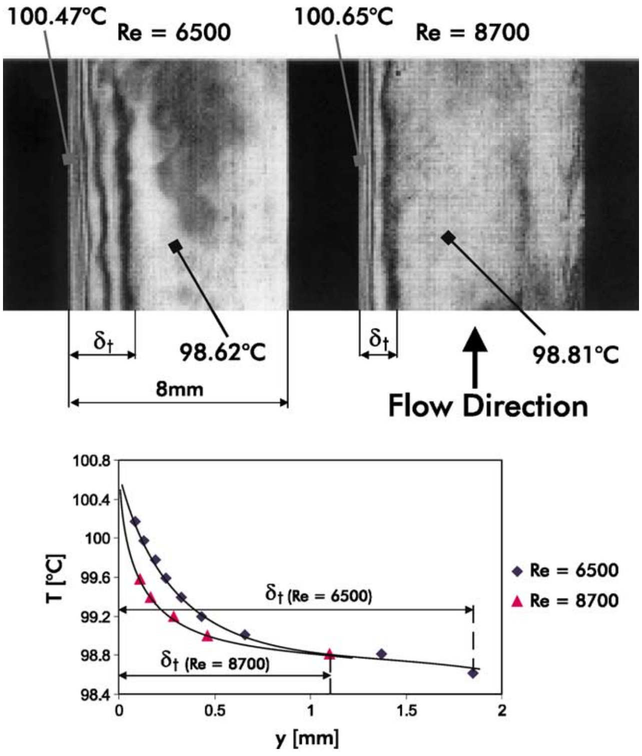

Fig. 6. Thermal boundary layer and temperature distribution at single-phase convection at various Reynolds numbers.

The diagram of Fig. 6 shows the evaluation of the interferograms. The interference fringes were converted into temperatures and were than plotted versus the distance of the wall. The thickness of the boundary layer was measured from the interferogram. As already described, the measurement points were approximated by a polynome function, and the temperature gradient at the wall was determined by differentiation of the polynome function with setting $y = 0$. It can be seen from the diagram that there are no measuring points in the immediate vicinity of the heated wall. This fact is due to the deflection of the laser light caused by the thermal boundary layer, as it is comprehensively described by Grigull and Hauf (1970), and Hauf et al. (1991), and the high fringe density in the thin fluid layer, as it is especially the case for $Re = 8700$, where the fringes can not be distinguished. The curve clearly shows that the temperature gradient is steeper at $Re = 8700$ than at $Re = 6500$. This results from the fact that the same amount of interference fringes are generated in a thinner boundary layer and therefore the distance between the fringes decreases. The local Nusselt number from the heated wall to the fluid is about $Nu = 31$ at $Re = 6500$ and $Nu = 44$ at $Re = 8700$. These values of the interferometrically obtained Nusselt numbers correspond very well with the values calculated from the Nusselt correlation of James et al. (1966) for one-sided heated rectangular channels.

3.2. Interaction between vapor bubble dynamics and thermal condition of the superheated liquid layer

In the following the change of the temperature field in the thermal boundary layer caused by a growing bubble is presented. Figs. 7 and 8 show a sequence of a bubble growing in the thermal boundary layer, detaching and condensing in the subcooled flow at $Re = 6500$ and $Re = 8700$, respectively. The diagrams next to the interferograms show the temperature distribution in the immediate vicinity of the bubble. The wall temperature is 104 °C. Owing to the high fringe density in the immediate region of the wall, only fringes up to 100 °C could be evaluated. The interferograms clearly show that the structure of the thermal boundary layer is affected by the growth and the detachment of the bubble.

The first interferograms ($t_1 = 0$ ms) of Figs. 7 and 8 show the bubble growing in the thermal boundary layer. At this point, the bubble is entirely surrounded by the thermal boundary layer. The temperature profile downstream of the bubble is shifted away from the wall which results from the stream conditions around the

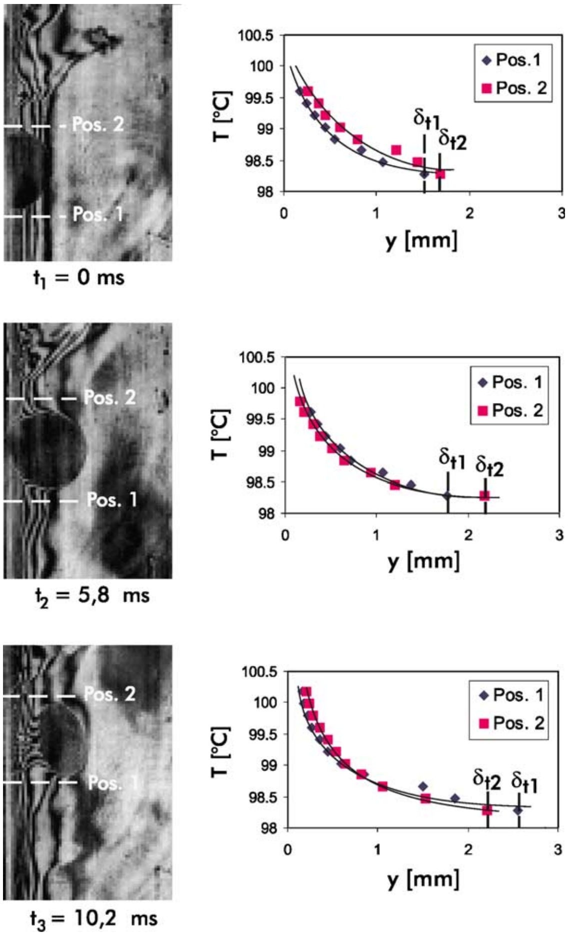

Fig. 7. Temperature distribution in the thermal boundary layer in the immediate vicinity upstream (Pos. 1) and downstream (Pos. 2) of the bubble at $Re = 6500$.

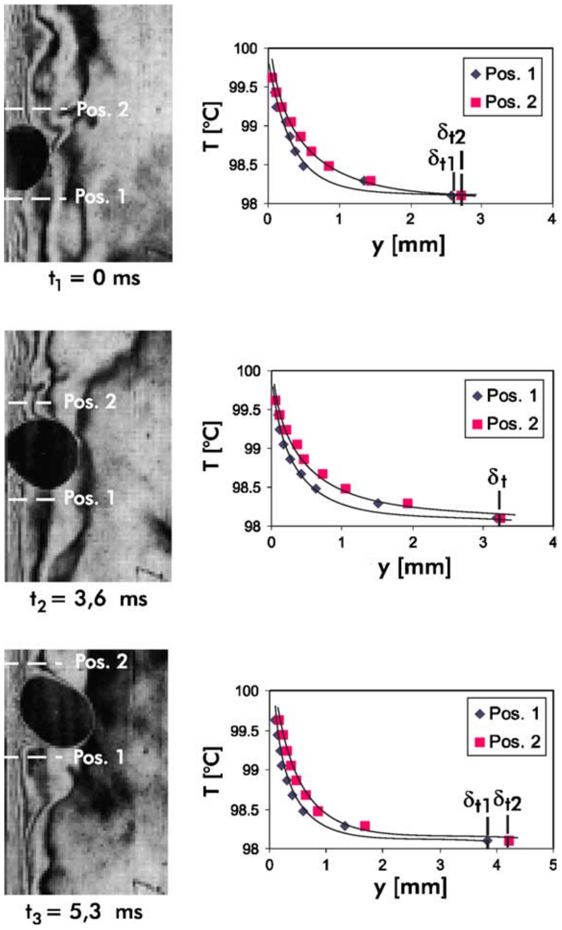

Fig. 8. Temperature distribution in the thermal boundary layer in the immediate vicinity upstream (Pos. 1) and downstream (Pos. 2) of the bubble at $Re = 8700$.

bubble. The liquid flowing around the bubble is decelerated downstream of the bubble head, the axial flow decreases and detaches then from the bubble surface. The boundary layer therefore is thicker than on the upstream side.

In the second diagram ($t_2 = 5.8$ ms, $t_2 = 3.6$ ms) of Figs. 7 and 8 the bubble grows out of the boundary layer while also moving along the heated wall. The bubble is constricted, and there is a remarkable deformation of the interference fringes along the bubble. At $Re = 6500$ the interference fringes downstream of the bubble are shifted towards the heated wall, and the temperature profiles downstream and upstream of the bubble are nearly identical. For $Re = 8700$ the temperature profiles of both positions are nearly identical in the immediate vicinity of the wall and in the outer thermal boundary layer, whereas the isotherms at the downstream side of the bubble within the boundary layer are shifted away from the wall. The reason for this effect is again the stream conditions around the bubble. The flow, as explained at $t_1 = 0$ ms, detaches from the bubble surface on the downstream side which has an impact on the temperature distribution.

At $t_3 = 10.2$ ms and $t_3 = 5.3$ ms, respectively, the bubble has left the thermal boundary layer and is condensing in the subcooled liquid. At $Re = 6500$ the bubble volume has remarkably decreased. It can also be seen that, for both Reynolds numbers, in the wake of the bubble hot fluid layers are dragged from the superheated boundary layer into the subcooled liquid. The superheated liquid layer in the immediate vicinity of the wall is reestablished, and the temperature gradient at the wall is steeper than that during the growth of the bubble deforming the interference fringes. When comparing the temperature profiles of both fluid velocities, it is also obvious, that the temperature gradient at the higher velocity is steeper which results in an enhancement of the heat transfer. The local Nusselt number in immediate vicinity of the bubble is about $Nu = 39$ at $Re = 6500$ and $Nu = 54$ at $Re = 8700$. Also these values are in very good agreement with the values obtained from the Nusselt correlation of James et al. (1966).

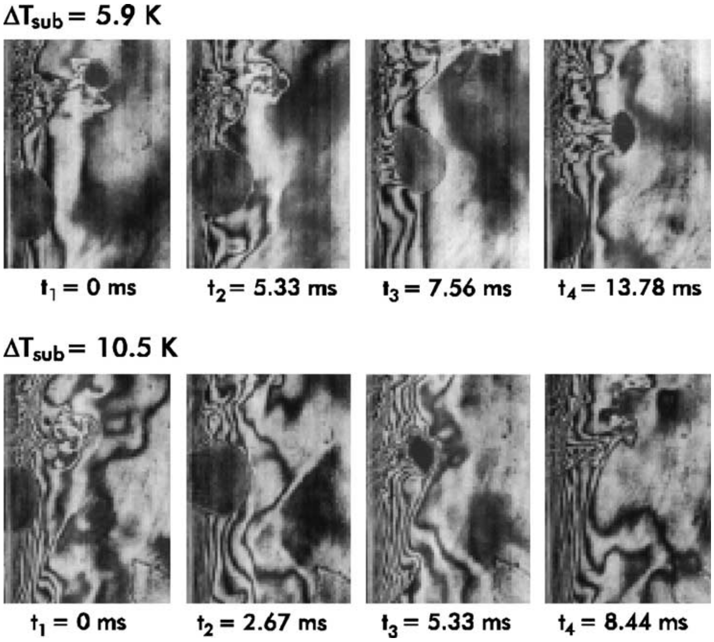

Fig. 9. Influence of the degree of subcooling on the thermo- and fluiddynamic behavior of a bubble ($Re = 6500$).

In Fig. 9 the impact of the degree of subcooling on the thermal boundary layer condition and the thermo- and fluiddynamic bubble behavior is presented. When comparing the sequences of both. $\Delta T = 5.9$ K and $\Delta T = 10.5$ K it is discernible that the fringe density in the boundary layer of the higher subcooling is higher due to the higher temperature difference between heated wall and fluid. The bubble grows into a steeper temperature gradient than that of the lower subcooling. From $t_1 = 0$ ms it can also be seen that the preceding bubble at a lower degree of subcooling has moved further into the fluid flow and has not condensed yet, whereas at the higher subcooling the preceding bubble has completely condensed at a shorter distance from the heated wall.

The second interferogram of both sequences ($t_2 = 5.33$ ms and $t_2 = 2.67$ ms) shows the bubble sliding along the heater surface while growing out of the thermal boundary layer, and the condensation process is induced at the head of the bubble. At the higher subcooling the bubble head is surrounded by a thicker boundary layer. This is due to the fact that at a higher subcooling the bubble condenses faster than in the warmer fluid and heat from the adjacent superheated liquid layer is not sufficiently supplied to maintain bubble growth. The flow around the bubble head stagnates, and therefore the heat which is released from the condensation process is stored at the phase-interface which in turn generates a thicker boundary layer and thus reduces the heat transfer, as also demonstrated by Nordmann and Mayinger (1981).

From the third interferograms ($t_3 = 7.56$ and 5.33 ms) it is also discernible that the wake of the detaching bubble from the superheated liquid layer is more turbulent than that of the warmer fluid. This results from the fast condensation of the bubble in the colder fluid which induces velocity fields due to the fast changing interface structure. The subcooled liquid flows into the void volume generated by the bubble condensation. This leads to an impulse impact against the bubble motion due to the fluid inertia, which is enhanced with the degree of subcooling, and fluid is pushed away in the wake. Owing to this process the bubble is subjected to pressure oscillations which in turn generate impulse reflections in direction of the bubble motion generating suction in the wake (see $t_4 = 8.44$ ms).

3.3. Impact of the fluid velocity and the degree of subcooling on the fluid- and thermodynamic behavior of a bubble

In the following the thermo- and fluiddynamic behavior of a single bubble is studied under the influence of the fluid flow velocity and the degree of subcooling of the liquid in order to assess the transferred heat energy due to bubble condensation.

Fig. 10 shows a temporal sequence of a bubble during its growth and condensation period. As also observed by Bibeau and Salcudean (1994), Zeitoun et al. (1995) as well as by Van Helden (1994), the bubble detaches from the cavity site shortly after nucleation and starts to slide a short distance along the heated wall while growing. It

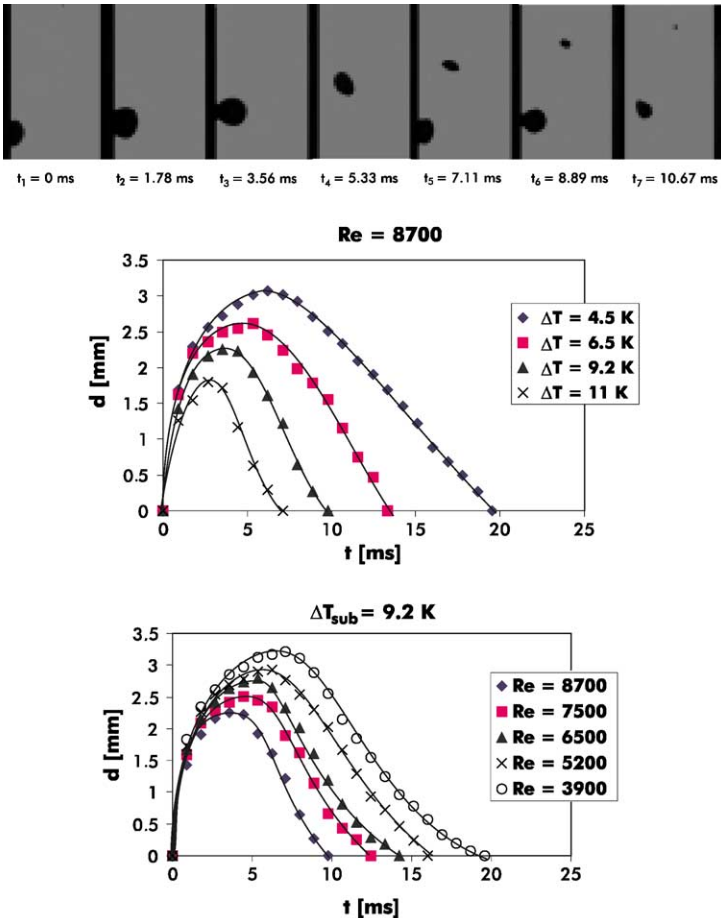

Fig. 10. Time-dependent bubble diameter at constant Reynolds number and constant degree of subcooling.

then detaches from the heated wall and is ejected into the subcooled liquid. The bubble collapses completely as it rises in the subcooled liquid, while it is subjected to a continuous change in shape due to the volume decrease and the flattening of the bubble head in movement direction.

The diagrams of Fig. 10 show the temporal development of the bubble diameter during bubble growth and condensation at a constant Reynolds number and at a constant subcooling, respectively. It can be seen from the diagrams that increasing the fluid velocity at constant subcooling as well as increasing the degree of subcooling at constant Reynolds number reduces the life-time of a bubble. It is also discernible that the temporal development of volume increase and decrease is not symmetrical which means that the temporal curve of the volume decrease is flatter than that of the volume increase. The condensation-time is longer than the bubble growth time which results from the big bubble volume and the relatively low subcoolings at which the heat transfer at the phase-interface governs the process.

Both diagrams also show that with higher fluid velocity or with higher subcooling the life-time curve approaches a more symmetrical shape, since the condensation of the smaller bubbles is a faster and more dynamic process. At very high degrees of subcooling the condensation process is very dynamic and therefore inertia-controlled, as it is illustrated by Mayinger (1982) and Nordmann and Mayinger (1981).

The maximum diameter of the bubble versus the Reynolds number at various degrees of subcooling is

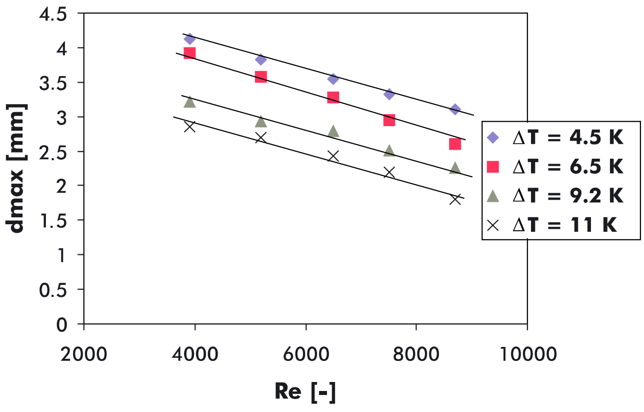

Fig. 11. Maximum diameter versus the Reynolds number at various degrees of subcooling.

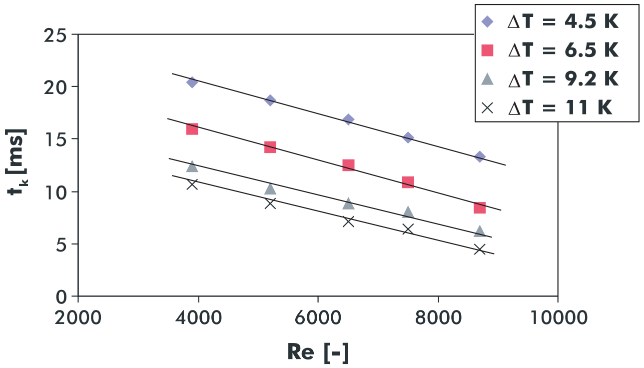

Fig. 12. Condensation-time versus the Reynolds number at various degrees of subcooling.

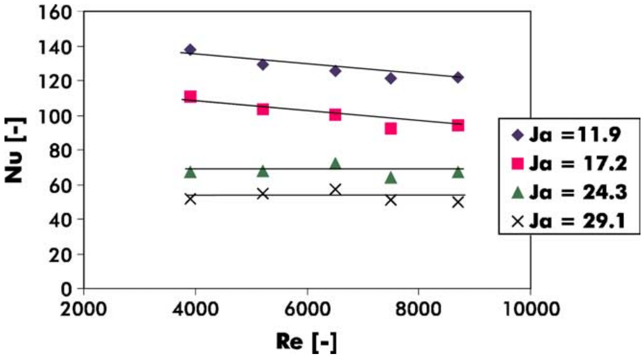

Fig. 13. Mean Nusselt number versus the Reynolds number at various Jakob numbers.

depicted in Fig. 11. As it can be seen the maximum diameter like the time-dependent diameter of a bubble is strongly governed by the fluid flow and the subcooling of the fluid, and it decreases with increasing the Reynolds number and the degree of subcooling.

Fig. 12 shows the condensation-time of a bubble versus the Reynolds number at various degrees of subcooling. As it can be seen, the condensation-time follows the same trend as the maximum equivalent diameter.

In subcooled boiling the Jakob number was introduced as the characteristic number which is based on the degree of subcooling ΔT_{sub} as the characteristic temperature difference:

$$Ja = \frac{\rho_{\mathrm{F}} c_P \Delta T_{\mathrm{sub}}}{\rho_V \Delta h_V} \tag{3.1}$$

The parameters of the liquid phase correspond to the liquid temperature, and the parameters of the vapor phase correspond to the saturation condition. The Jakob number gives the ratio of the lacking energy of the fluid to reach the saturation point and the stored energy of the vapor at the same volume. The Jakob number considers the pressure in a system and thus enables the comparison of experimental data from the literature at the same Jakob number. Furthermore, it determines the effect that governs the collapse of a bubble during the condensation. Chen and Mayinger (1992) showed that for $Ja < 60$ the bubble collapse is entirely controlled by the interfacial heat transfer, whereas for higher Jakob numbers the inertia of the liquid mass governs the process. As it will be seen in the following, this study is focussed on the heat transfer controlled condensation process.

For the determination of the interfacial heat transport of a bubble to the fluid, the mean heat transfer coefficient α averaged over the bubble circumference and the condensation-time is calculated from the energy balance such that the condensation heat released by the volume decrease equals the heat transferred to the fluid.

$$\alpha = \frac{\rho_{\mathrm{D}} V_0 \Delta h_V}{0.5 A_0 (T_{\mathrm{S}} - T_\infty) t_K} \tag{3.2}$$

where V_0 is the maximum volume of the bubble, A_0 the surface of the bubble, and t_k the condensation-time of the bubble.

In Fig. 13 the mean Nusselt number between bubble and fluid is plotted versus the Reynolds numbers at various Jakob numbers. As it can be seen, the Nusselt number decreases with increasing the Jakob number which is only governed by the degree of subcooling in this study, since the pressure was constant during the experiments. This means that at higher Jakob number and therefore higher subcooling, the bubble volume decreases, as it is depicted in Fig. 11, and thus the mass of the vapor which releases heat energy during the condensation process.

It can also be seen that within this range of Reynolds numbers, the fluid velocity does not have an impact on the mean Nusselt number, and the transferred heat from a single bubble to the liquid remains approximately constant. As it has been described above, the heat transfer coefficient is based on the energy balance of stored and transferred heat where the governing parameters are the bubble size and the condensation-time.

3.4. Local heat transfer at the phase-interface between bubble and subcooled liquid

In the following the local Nusselt number over the perimeter at various angles of a bubble was determined using the finitefringe method. The degree of subcooling is $\Delta T = 6.1$ K and the fluid velocity is $w = 0.08$ m/s which corresponds to $Re = 2400$. Fig. 14 shows a sequence of interferograms of a bubble growing in the thermal boundary layer ($t_1 = 0$ ms) and then growing out of the boundary layer while still attached to the heated wall ($t_2 = 1.33$ ms and 3.11 ms).

In the first interferogram ($t_1 = 0$ ms) the bubble head is surrounded by a relatively thick thermal boundary

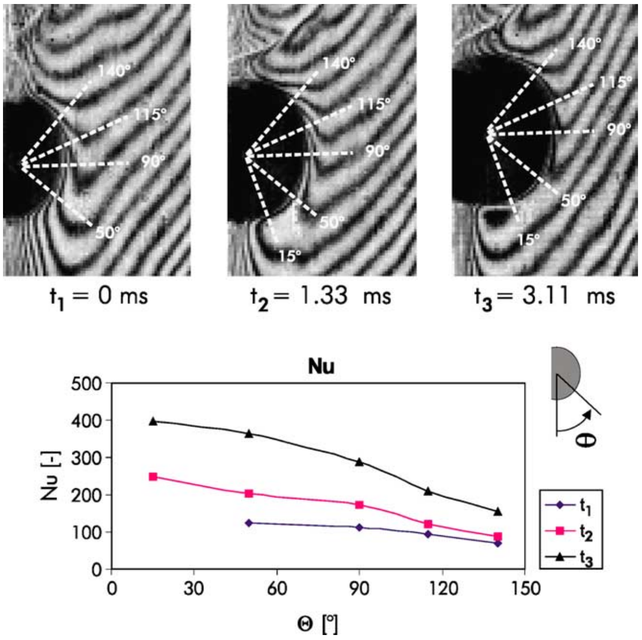

Fig. 14. Local Nusselt number versus the perimeter of a growing bubble at various angles.

layer. This condition is reflected in the Nusselt curve. The Nusselt number is the lowest at this stage and it decreases slightly with the angle of the perimeter.

The second interferogram ($t_2 = 1.33$ ms) shows the bubble growing out of the superheated liquid layer. The boundary layer thickness at the phase-interface has decreased. It is the thinnest at 15° and increases with the perimeter in downstream direction. The boundary layer conditions around the bubble stem from the stream conditions around the bubble. The fluid passes the bubble and is decelerated downstream of the bubble head. The axial flow decreases and detaches from the bubble surface on the downstream side which results in a thicker boundary layer. These conditions are also confirmed by the Nusselt curve. The heat transfer is the highest in the region of the incoming flow and decreases along the perimeter in downstream direction. The enhancement of the heat transfer compared to the first stage of the bubble ($t_1 = 0$ ms) results from the fact that the bubble, while still attached to the heated wall and receiving heat from the adjacent superheated liquid layer, condenses at the head and therefore releases the heat directly to the subcooled fluid.

At the third stage of the bubble ($t_2 = 3.11$ ms) the bubble has remarkably increased in size, and a very thin boundary layer is discernible at the phase-interface which means that heat is transferred at the phase-interface while heat from the superheated liquid layer is sufficiently supplied to maintain bubble growth. The increase of the bubble volume and decrease of the boundary layer lead to a further increase of the Nusselt number, as it is depicted in the diagram.

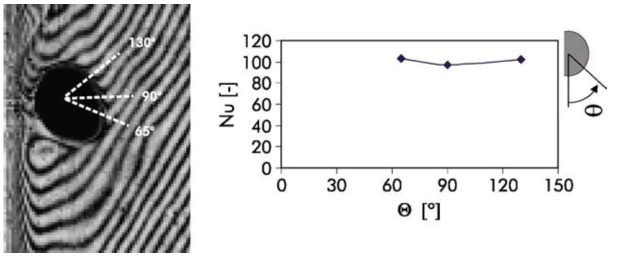

Fig. 15. Local Nusselt number versus the perimeter of a detaching bubble at various angles.

Fig. 15 shows the bubble detached from the superheated liquid layer and entirely surrounded by the subcooled liquid. The volume has decreased and the bubble does not receive energy from the superheated liquid layer any more. The bubble head is surrounded by a thick thermal boundary layer. The reason for this effect is, as already described before, that heat is released during the condensation process, while no further energy is supplied to the bubble. The volume decreases and the bubble head is flattened due to the drag force which interrupts the flow around the bubble and generates a thicker boundary layer and thus reduces the heat transfer. This effect is confirmed by the significant decrease of the Nusselt number compared to those in Fig. 14. As it can be seen, the Nusselt number could only be determined in a very restricted region which is determined by the fringe pattern setting.

Therefore no information about the heat transport at the upstream and downstream side of the bubble is given here. In the measured region the Nusselt number is approximately constant. The investigations of the local Nusselt number are, considering the experimental conditions and parameters, in good agreement with the results of Chen and Mayinger (1985, 1992) and Nordmann and Mayinger (1981).

4. Numerical techniques and results

In order to simulate scenarios such as the ones described in the experimental part of this article, we now present a numerical scheme on the basis of a Lagrangian description of the bubbles which is linked to a numerical solution of the Navier–Stokes equations on orthogonal grids. Since the shape of the bubbles is only poorly described by cells of an orthogonal grid, modeling of the influence of the bubbles on the surrounding fluid is done by modifying the body force term. Successful simulations of this type are reported by Maxey et al. (1997) and Xu et al. (2002), as well as by Tomiyama et al. (1997). In the papers by Maxey et al. (1997) and Xu et al. (2002), the bubble Reynolds number is very low such that the hypothesis of Stokes is true, and the force exerted by the bubble on the surrounding fluid can be calculated by the solution of the Stokes equation. This is used to calculate an appropriate value for the discrete body force term. Here the bubble Reynolds numbers are significantly higher. From literature no general data of flow fields around such bubbles rising in a stagnant fluid (corresponding to the case of Stokes flow) are known, see Oliver and Chung (1987). We were therefore forced to determine the correct lift force by numerical experiments in order to have at least macroscopic quantities mapped correctly into the numerical scheme.

For the simulation of the flow field of the liquid phase the Navier–Stokes equations are approximately solved by a finite-volume-scheme which is explicit in time. Discretization in space and time ensures second order of accuracy. Turbulence is modeled by a LES method on basis of the Smagorinsky approach. The Smagorinsky coefficient is calculated dynamically following the scheme of Germano et al. (1991) and Lilly (1992). The method is stabilized by averaging along streamlines as proposed by Meneveau et al. (1996) such that no lines, planes or sites of homogeneous turbulence are needed for the averaging procedure. It should be outlined that this is crucial for the application of LES in two-phase flow problems of the type studied.

In our method the influence of the bubbles on the flow field is entirely modeled by calculating the body force term in the Navier–Stokes equations. The bubbles are assumed to be spherical or ellipsoidal. As it can be seen from Grace (1973) there is no serious restriction of possible fields of application, since Eötvös Numbers lower than 10 cover a wide range of possible media combinations and bubble shapes. This allows the description of the bubbles by only six parameters (three axis lengths and three rotation angles) in addition to the coordinates of the bubble center. The influence of the bubbles on the flow field is considered by determining the body force term in the Navier–Stokes equations based on the density field which is calculated with respect to the position and shape of the bubbles. This is done before each time step of the explicit integration scheme in time. After the time step the new positions and shapes of the bubbles are calculated from the new velocity field, and are therefore available for the calculation of the next density field. The scheme is displayed in Fig. 16.

Gas/liquid systems are characterized by the large difference between gas and liquid phase. Therefore the assumption that the density of the gaseous phase is small compared to the density of the liquid.

$$\rho_1 >> \rho_2 \tag{4.1}$$

is used here for simplicity. The body force in the continuous Navier–Stokes equations, f^+ (force per volume) can reach two values:

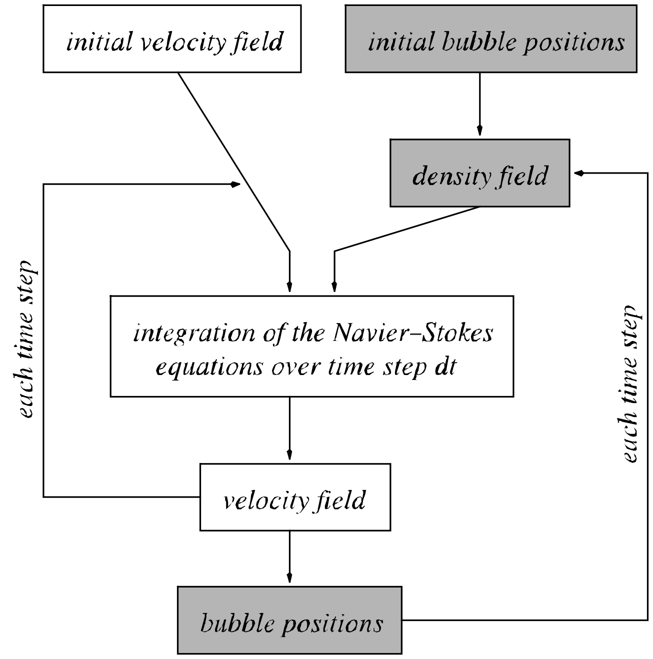

Fig. 16. Scheme of the coupled simulation procedure.

$$\begin{aligned} f^+(x,y,z) &= 0 \quad \text{if } (x,y,z) \text{ inside a bubble} \\ f^+(x,y,z) &= g^+ \quad \text{elsewhere} \end{aligned} \tag{4.2}$$

where g^+ denotes the gravity vector. The discretization brings about that the body force term has to be calculated at the grid points. Evaluating it at grid points by inserting coordinates of grid points into Eq. (4.2) cannot be accurate because the lift force exerted by a single bubble would depend on the position of the bubble relative to the grid, if there are cells containing both, gas and liquid. For those cells the body force term is therefore calculated from the information of the position and shape of the bubbles according to

$$f_i = \frac{1}{V} \int_{(V)} f^+(x,y,z)\,\mathrm{d}V \tag{4.3}$$

where f_i is the value of the body force term at a certain grid point addressed by the subscript i. The integral is evaluated using the method of Gauss–Legendre. For all cells containing only a single-phase, Eq. (4.2) is used to determine the body force term.

The six parameters describing the shape and the orientation of the bubbles are to be determined such that the potential energy of deformation is at its minimum, i.e. equilibrium is assumed. This is the case if the term equals 0:

$$\begin{aligned} \Delta W &= \left| \int_{(A)} \left[(p_2 - p_1) - \gamma \cdot \left(\frac{1}{R_\varphi} - \frac{1}{R_\theta} \right) \right] \cdot \Delta x\,\mathrm{d}A \right| \\ &= 0 \quad \forall \Delta x(\xi,\eta) \in V \subset C^1 \end{aligned} \tag{4.4}$$

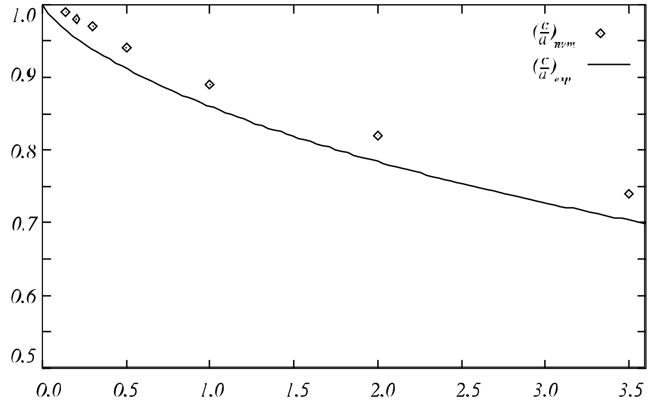

Fig. 17. Comparison between numerically found ratio of axis lengths of an ellipsoidal bubble rising in initially stagnant infinitely extended liquid versus Eötvös number.

Here p_1 denotes the pressure in the outer phase, p_2 the pressure in the gas, R_φ and R_θ are the main radii of curvature of the phase-interface, and depend (as do the pressures) on local surface coordinates ξ and η. Δx is the potential deformation; it is a continuous function, and it is assumed (in this weak formulation of the equilibrium condition) to be taken from some function space V.

The axis lengths and rotation angles describing the ellipsoid are now determined by minimizing the integral in (4.4) by variation of these six parameters where the integrand is evaluated at 18 representative points on the ellipsoidal surface. From Fig. 17 it can be seen that the prediction of the shape of the bubbles is in rather good agreement with observations collected by Wellek et al. (1966) for the case of bubbles rising in infinitely extended ocean initially at rest.

The new position of the bubble is determined by translating the bubble by a distance of time step multiplied by a velocity vector which is set to be the average velocity vector within the portion of space occupied by the actual bubble.

The simplicity of the model makes it impossible to keep the boundary conditions exact. The calculated terminal rise velocity of the bubbles in infinitely extended stagnant ocean is therefore usually misinterpreted. However, we found that there is a correlation between this error and the ratio of bubble size and grid spacing. This correlation is exploited to determine a correction factor α which ensures the terminal rise velocity of the bubbles to be predicted correctly. The body force term is then modified according to

$$f_i = \alpha \cdot f_i^* \tag{4.5}$$

The correlation between the error and the ratio of bubble size and grid spacing depends also on the bubble Reynolds number and the position of the bubble relative to the computational grid.

In a few typical cases we shall now demonstrate the good prediction properties of the proposed method. This is done by comparing the numerical results to experimental data of Lucic et al. (2001). The experimental set-up is an open loop comprising a vertical transparent channel of rectangular cross-section with stagnant liquid as well as with pressure driven upward flow with a bulk velocity of $u = 0.4$ m/s ($Re = 5300$). In this case the flow is turbulent. In order to avoid the expenses of the simulation of the part of the channel where turbulence is developing we consider only the part of the channel where the bubbles are actually present. In the inflow face of the computational domain the boundary conditions have to account for the turbulent flow. This is archived by taking the velocities at the inflow face to be the instantaneous velocities in one cross-section of a second simulation of the single-phase flow in the same channel with periodic boundary conditions in vertical direction (see Fig. 18).

In the experiment the bubbles are generated by injecting air at a volume flux of 40 ml/min through a single orifice of the side-wall of the vertical channel into the test fluid water. Fig. 19 shows that the prediction of the rise velocities versus the vertical distance to the orifice is satisfactory in these cases.

As it can be seen from the comparison, the numerical and experimental results have larger differences for the highest bulk velocity (top curve) which diminish with

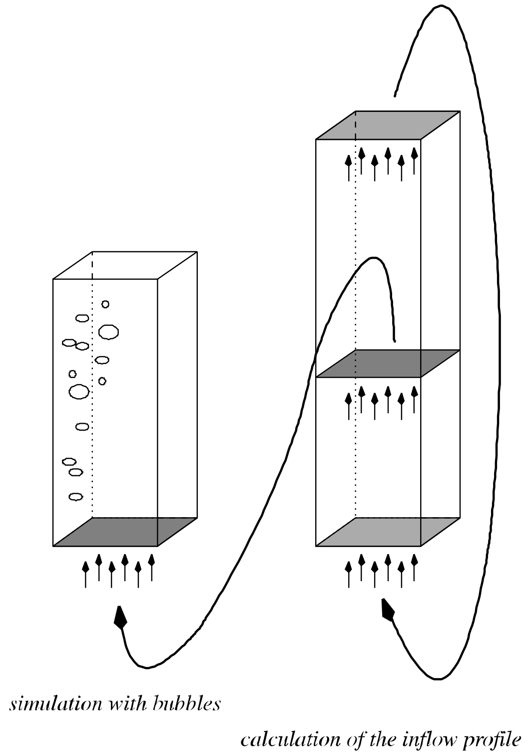

Fig. 18. Generation of a turbulent inflow condition for the numerical simulation.

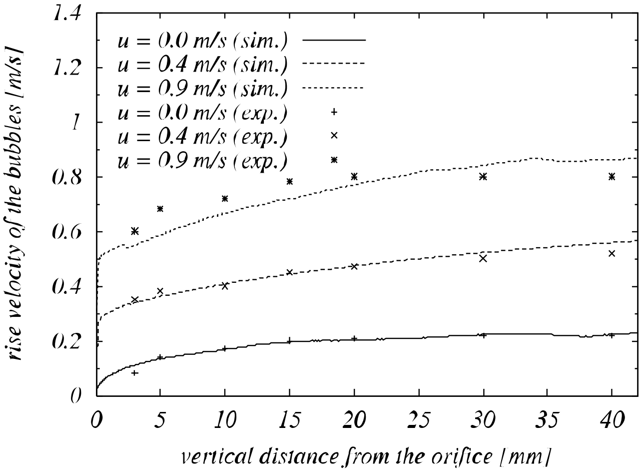

Fig. 19. Comparison between simulation and experiment: bubble rise velocities in the case of stagnant liquid and turbulent flow versus the vertical distance from the wall.

decreasing the bulk velocity. This results from the fact, that the prediction of the bubble velocity becomes less accurate with increasing the bulk velocity. This in turn is due to the properties of the LES model which interferes with the bubble model.

In a second comparison between experiment and calculation, a similar scenario is considered. It can be demonstrated that also the flow field is predicted correctly by the numerical procedure. The velocity in the direction of the channel axis (z-direction) in a vertical distance of 16 mm of the orifice is plotted as a function of the perpendicular distance to the wall for the same configuration where $u = 0.3$ m/s ($Re = 4000$) and the gas volume flux is 16 ml/min. The comparison between experiment and simulation again shows good agreement, as it can be seen from Fig. 20.

The potential of the prediction of the flow field seems to predestine this method for the simulation of heat flux phenomena near heated walls. Therefore the numerical method has been expanded to the approximate solution of a transport equation of the temperature. The modeling of turbulence applied to the velocity field has been expanded to the heat transport. The same discretization grid is used. Due to high additional computational cost a dynamical method for the determination of the turbulent Prandtl number has been replaced by a static model where this number is assumed to be 0.4 everywhere as it is described in Grötzbach and Wörner (1999). The bubble model here accounts for bubble growth and bubble volume decrease determining the bubble size from a balance of thermal energy in the vicinity of the bubble. The bubble size is calculated such that all the fluid in the volume, comprising the bubble itself as well as its vicinity, is at boiling temperature. Within the spatial resolution of the discretization grid this is a good approximation which becomes exact as grid spacing and time step approach zero. Again the results of experiment and numerical simulation are compared. The boundary conditions of the numerical simulation have been chosen in accordance to the experiments described in Section 3. In Figs. 21 and 22 the spatially resolved temperature field in the vicinity of a vapor bubble which is growing and detaching in the thermal boundary layer are shown.

Fig. 21 shows the simulated temperature field in the vicinity of a growing bubble in comparison to the interferometrically measured temperature field as it has been realized with the infinite-fringe method. It can be seen that the increased thickness of the thermal boundary layer in downstream direction of the bubble is visible in both, experiment and numerical simulation. The simulated bubble shape and size, however, differ

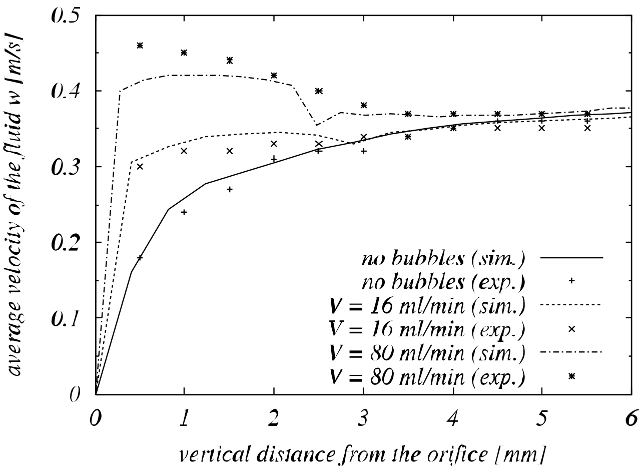

Fig. 20. Comparison between simulation and experiment: average velocity in z-direction as a function of the distance from the wall for single-phase flow and flow in the presence of bubbles.

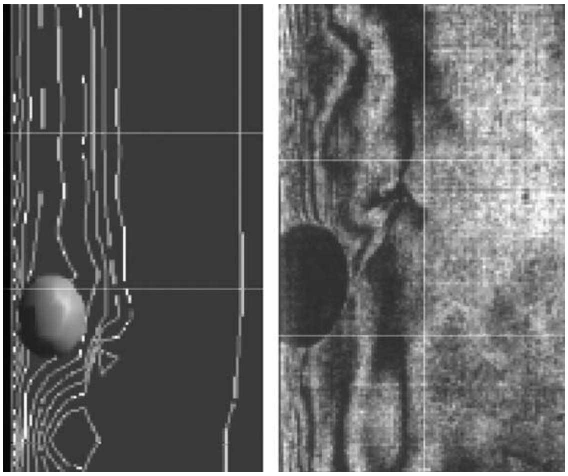

Fig. 21. Comparison between simulation and experiment: spatially resolved temperature field around a vapor bubble growing in the thermal boundary layer.

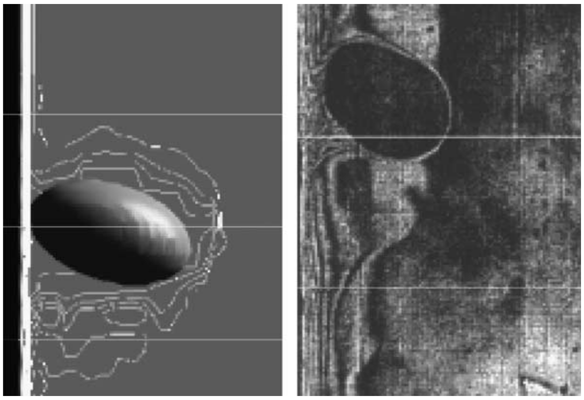

Fig. 22. Comparison between simulation and experiment: spatially resolved temperature field around a vapor bubble after detachment from the cavity site.

from the real bubble which stems from the fact, that the used model does not consider the complex process of bubble growth at the heated wall.

Fig. 22 illustrates a bubble which is detached from the cavity site at the wall. The bubble shape in both numerical simulation and experiment deviates remarkably from the spherical shape. The slight asymmetry of the real bubble, as it can be seen from the interferogram, could not be realized in the simulation owing to the restriction to the ellipsoidal shape. The direction and the axes ratio of the simulated bubble however show that the used model could approximate the bubble shape satisfyingly.

Furthermore, the boundary layer conditions around the bubble can be clearly seen in the simulated temperature field, whereas in the experiment the thin boundary layer around the bubble could not be resolved by the finite-fringe method, as it has been described previously.

However, the situation in the wake of the bubble is not mapped satisfyingly in the numerical simulation. This seems to be due to the fact that the resolution of the discretization grid at the wall is not fine enough to resolve the flow between the bubble and the wall which is responsible for the temperature field pattern in the wake of the bubble as it is observed in the experiment. The fact that the ellipsoidal bubble shape is just an approximation to the physical bubble shape increases the error.

5. Conclusion

In this study measurements by means of the optical technique holographic interferometry and numerical simulations were performed to demonstrate the interaction of a vapor bubble, which grows in the thermal boundary layer and condenses in the subcooled fluid, and the forced bulk convection.

The holographic interferometry enabled the visualization of the inhomogeneous temperature field of the thermal boundary layer of the flowing subcooled liquid in the presence of a vapor bubble and the visualization of the temperature field around the vapor bubble during the growth and condensation process. Thus the impact of the fluid velocity and the degree of subcooling on the interaction of the fluid- and thermodynamic behavior of the bubble and the thermal boundary layer could be determined.

By evaluating the visualized temperature field in the immediate vicinity of the bubble, the local heat transfer at the phase-interface between bubble and subcooled liquid at various positions along the bubble perimeter could be quantified.

The proposed numerical method has shown to yield results in good quantitative agreement with the experiments. Fluid dynamical as well as thermal processes are predicted satisfyingly. Therefore this method is hoped to allow numerical simulations of phenomena in heat transfer at heated walls which are not accessible to current measurement techniques.

It could prove to be capable of finding answers to some open questions in this field as to what extent latent heat transfer contributes to the total heat transfer rate.

References

Bibeau, E.L., Salcudean, M., 1994. A Study of bubble ebullition in forced-convective subcooled nucleate boiling at low pressure. Int. J. Heat Mass Transfer 37 (15), 2245–2259.

Chen, Y.-M., 1985. Wärmeübergang an der Phasengrenze kondensierender Blasen. Dissertation, Technische Universität München.

Chen, Y.-M., Mayinger, F., 1985. Holographic interferometry studies of the temperature field near a condensing bubble. In: Pichal, M. (Ed.), Optical Methods in Dynamics of Fluid and Solids, Proc. of an int. Symposium, September 17–21, 1984, IUTAM. Springer-Verlag, Berlin.

Chen, Y.-M., Mayinger, F., 1992. Measurement of heat transfer at the phase-interface of condensing bubbles. Int. J. Multiphase Flow 8 (6), 877–890.

Esmaeeli, A., Tryggvason, G., 1998. Direct numerical simulation of bubbly flows. Part I: low Reynolds number arrays. J. Fluid Mech. 377, 313–345.

Esmaeeli, A., Tryggvason, G., 1999. Direct numerical simulation of bubbly flows. Part II: low Reynolds number arrays. J. Fluid Mech. 385.

Gabor, D., 1951. Microscopy by reconstructed wavefronts II. Proc. Royal Soc. B 64.

Germano, M., Piomelli, U., Moin, P., Cabot, W., 1991. A dynamic subgrid-scale eddy viscosity model. Phys. Fluids A 3, 1760–1765.

Göz, M., Bunner, B., Sommerfeld, M., Tryggvason, G., 2002. Direct numerical simulation of bubble swarms with a parallel front-tracking method. In: High Performance Scientific and Engineering Computing. Springer-Verlag, Berlin.

Grace, J., 1973. Shapes and velocities of bubbles rising in infinite liquids. Trans. Inst. Chem. Eng. 51, 116–120.

Grigull, U., Hauf, W., 1970. Optical methods in heat transfer. In: Advances in Heat Transfer, vol. 6. Academic Press, New York. pp. 133–366.

Grötzbach, G., Wörner, M., 1999. Direkt numerical and large-eddy simulations in nuclear applications. Int. J. Heat Fluid Flow 20, 222–240.

Hauf, W., Grigull, U., Mayinger, F., 1991. Optische Meßverfahren in der Wärme- und Stoffübertragung. Springer-Verlag, Berlin.

Hirt, C., Nichols, B., 1981. Volume of fluid (VoF) method for the dynamics of free boundaries. J. Comput. Phys. 39, 201–235.

James, D.D., Martin, B.W., Martin, D.G., 1966. Forced convection heat transfer in asymmetrically heated ducts of rectangular cross-section. In: Proc. of the 3rd Int. Heat Transfer Conference, vol. 1, pp. 85–98.

Kanai, A., Miyata, H., 2001. Direct numerical simulation of wall turbulent flows with microbubbles. Int. J. Numer. Meth. Fluids 35, 593–615.

Lilly, D., 1992. A proposed modification of the germano subgrid-scale method. Phys. Fluids A 4, 633–635.

Lucic, A., Mayinger, F., Meier, F., Zenger, C., 2001. Experimental study and numerical simulation of the velocity field around rising bubbles in stagnant and flowing liquid. In: Proc. of the 2nd International Conference on Computational Heat and Mass Transfer, Rio de Janeiro, Brasil.

Maxey, M.R., Patel, B.K., Chang, E.J., Wang, L.P., 1997. Simulations of dispersed turbulent multiphase flow. Fluid Dyn. Res. 20, 143–156.

Mayinger, F., 1982. Strömungen und Wärmeübergang in Gas-Flüssigkeits-Gemischen. Springer-Verlag, Berlin.

Mayinger, F., 2000. Optical Measurements. Springer-Verlag, Berlin.

Meneveau, C., Lund, T., Carbot, S.W.H., 1996. A lagrangian dynamic subgrid-scale model of turbulence. J. Fluid Mech. 319, 353–385.

Nordmann, D., Mayinger, F., 1981. Temperatur, Druck und Wärmetransport in der Umgebung kondensierender Blasen, VDI Forschungsheft. VDI-Verlag, Düsseldorf. p. 605.

Oliver, D.L.R., Chung, J.N., 1987. Flow about a fluid sphere at low to moderate Reynolds numbers. J. Fluid Mech. 177, 4–18.

Panknin, W., 1977. Eine holographische Zweiwellenlängen-Interferometrie zur Messung überlagerter Temperatur- und Konzentrationsgrenzschichten. Dissertation, Universität Hannover.

Qiu, D., Dhir, V.K., 1999. An experimental study of heat transfer during sliding bubbles on inclined surfaces. In: Proc. of 5th ASME/JSME Thermal Engineering Conference, San Diego, USA.

Socholichin, A., Eigenberger, G., 1994. Gas–liquid flow in bubble columns and loop reactors. Part I: detailed modelling and numerical simulations. Chem. Eng. Sci. 49, 5735–5746.

Socholichin, A., Eigenberger, G., 1999. Application of the standard κ-epsilon turbulence model to the dynamic simulation of bubble columns. Part I: detailed numerical simulations. Chem. Eng. Sci. 54, 2273–2284.

Tomiyama, A., Zun, I., Higaki, H., Makino, Y., Sakaguchi, T., 1997. A three-dimensional particle tracking method for bubbly flow simulation. Nucl. Eng. Des. 175, 77–86.

Tryggvason, G., Bunner, B., Esmaeeli, D., Juric, D., Al-Rawahi, N., Tauber, W., Han, J., Nas, S., Jan, Y.-J., 2001. A front-tracking method for the computations of multiphase flow. J. Comput. Phys. 169, 708–759.

Van Helden, W.G.J., 1994. On detaching bubbles in upward flow boiling. Dissertation, Technische Universität Eindhoven, Netherlands.

Wellek, R.M., Agrawal, A.K., Skelland, A.H.P., 1966. Shape of liquid drops moving in liquid media. AIChE J., 12.

Xu, J., Maxey, M.R., Karniadakis, G., 2002. Numerical simulation of turbulent drag reduction using microbubbles. J. Fluid Mech. 408, 271–281.

Zeitoun, O., Shoukri, M., Chatoorgoon, V., 1995. Interfacial heat transfer between steam bubbles and subcooled water in vertical upward flow. J. Heat Transfer-Trans. ASME 117, 402–407.